Check for updates

Spectroscopic Evidence of Intraband Gap States in α-$SnWO_4$ Photoanodes Introduced by Interface Oxidation

*Patrick Schnell, Erwin Fernandez, Keisuke Obata, Jennifer Velázquez Rojas, Marco Favaro, Thomas Dittrich, Roel van de Krol, and Fatwa F. Abdi**

α-$SnWO_4$ is an emerging photoelectrode material for photoelectrochemical water splitting, with several promising properties such as the favorable bandgap of 1.9 eV and suitable positions of the valence and conduction band. However, a major challenge remains: unprotected α-$SnWO_4$ undergoes surface passivation that blocks further charge transfer, and α-$SnWO_4$ electrodes that are covered with a protection/catalytic overlayer (e.g., NiO_x, CoO_x) show limited photovoltage. Earlier studies reveal that interfacial oxidation occurs due to the deposition of the overlayer. This negatively impacts the photovoltage that can be extracted, which is attributed to Fermi-level pinning at the interface. The exact origin of this Fermi-level pinning mechanism, however, remains unclear. In the present study, a combination of surface photovoltage analysis and hard X-ray photoelectron spectroscopy is used to elucidate the electronic structure of the α-$SnWO_4$/oxide interface. Both techniques offer compelling and consistent evidence for the presence of a defect state that is energetically located within the bandgap energy of α-$SnWO_4$ and is likely responsible for the Fermi-level pinning.

1. Introduction

The importance of renewable hydrogen has been increasingly promoted in the efforts to decarbonize our fossil-fuel-dependent society. One approach to generate renewable hydrogen is via photoelectrochemical water (PEC) splitting, where photon energy from sunlight is directly used to split water into hydrogen and oxygen. The process utilizes cheap and abundant feedstocks (i.e., water and sunlight) and may therefore provide a substantial contribution to a renewable, carbon-free energy system. In PEC water splitting, sunlight is absorbed by semiconductor photoelectrodes to generate charge carriers (electrons and holes), which then reduce and oxidize water to generate hydrogen and oxygen, respectively.[1–4] Several classes of semiconducting materials have been investigated, but none of the materials have satisfied all the necessary requirements for highly efficient and stable photoelectrodes. For example, classical semiconductors such as Si or III–V semiconductors possess excellent carrier transport properties, but they are unstable in aqueous electrolytes.[5,6] Metal oxide semiconductors show much better stability, are potentially cheaper, and are easier to process, but most of them show modest light absorption and/or have poor carrier transport properties.[7–9] The search for a highly efficient metal oxide photoelectrode is therefore one of the main challenges currently faced by the PEC community.

With all possible compositions of binary metal oxides having been experimentally explored, the focus has been shifted to more complex metal oxides (i.e., ternary or quaternary). An emerging material in this class of material is α-$SnWO_4$. It has an orthorhombic crystal structure with the unit cell composed of Sn tetrahedra and W octahedra. The material shows n-type conductivity, which means that it should be employed as the photoanode in PEC water splitting devices. Several studies have been reported in the last few years on α-$SnWO_4$ films prepared by different techniques,[10–22] e.g., hydrothermal synthesis, reactive magnetron sputtering, pulsed laser deposition, and chemical vapor deposition. The attractive properties of this material as a photoanode include the bandgap of 1.9 eV, which is close to ideal for use as a top absorber in a tandem configuration, and the favorably low onset potential of $\approx$0 V versus RHE.[11,14,16,23] The highest reported AM1.5 photocurrent is $\approx 1\ \mathrm{mA\ cm^{-2}}$,[24] which is still far from the theoretical maximum of $\approx 17\ \mathrm{mA\ cm^{-2}}$ (assuming that all sunlight photons with energy beyond the bandgap of α-$SnWO_4$ are utilized). Our previous studies on pulsed laser deposited α-$SnWO_4$, as well as studies by others on this material, have shed light on two major limitations. The first limitation is related to the charge carrier transport

P. Schnell, E. Fernandez, K. Obata, J. V. Rojas, M. Favaro, R. van de Krol, F. F. Abdi
Institute for Solar Fuels
Helmholtz-Zentrum Berlin für Materialien und Energie GmbH
Hahn-Meitner-Platz 1, 14109 Berlin, Germany
E-mail: fatwa.abdi@helmholtz-berlin.de

P. Schnell, E. Fernandez, J. V. Rojas, R. van de Krol
Institut für Chemie
Technische Universität Berlin
Straße des 17. Juni 124, 10623 Berlin, Germany

T. Dittrich
Institute for Silicon Photovoltaics
Helmholtz-Zentrum Berlin für Materialien und Energie GmbH
Schwarzschildstr. 8, 12489 Berlin, Germany

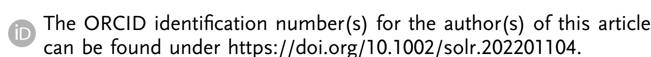
The ORCID identification number(s) for the author(s) of this article can be found under https://doi.org/10.1002/solr.202201104.

© 2023 The Authors. Solar RRL published by Wiley-VCH GmbH. This is an open access article under the terms of the Creative Commons Attribution License, which permits use, distribution and reproduction in any medium, provided the original work is properly cited.

DOI: 10.1002/solr.202201104

2367198x, 0, Downloaded from https://onlinelibrary.wiley.com/doi/10.1002/solr.202201104 by Weizmann Institute Of Science, Wiley Online Library on [07/02/2023]. See the Terms and Conditions (https://onlinelibrary.wiley.com/terms-and-conditions) on Wiley Online Library for rules of use; OA articles are governed by the applicable Creative Commons License

properties. Grain boundaries have been reported to limit charge transport,[10] and the transport properties are reported to be highly anisotropic.[18,25] Epitaxial or highly oriented films are therefore expected to have much improved charge transport, and indeed recent reports on two-dimensional α-$SnWO_4$ crystalline nanosheets with preferred {001} orientation demonstrated superior performance.[18–20] Another limitation is the modest photovoltage that can be extracted from the material, despite the fact that the band positions straddle the water reduction and oxidation potentials (which would enable a maximum quasi-Fermi level splitting of at least 1.23 V under operating conditions). In our earlier study on NiO_x-coated α-$SnWO_4$, in which the NiO_x serves as the protection layer, we showed that the limitation of the photovoltage can be correlated with the formation of an interfacial oxide layer at the interface of α-$SnWO_4$ and NiO_x.[12] A similar observation of limited photovoltage has been reported for CoO_x-coated α-$SnWO_4$.[21] The interfacial layer contains Sn^{4+}, most likely in the form of SnO_2, which adversely affects the charge transfer at the interface. Fermi-level pinning due to the presence of intraband states was suggested as the possible underlying mechanism of the limitation in photovoltage.

In this study, we utilize spectroscopic techniques to further unravel the presence of such intraband states. Surface photovoltage (SPV) analysis reveals the wavelength-dependent photovoltage response of α-$SnWO_4$ and synchrotron-based hard X-ray photoelectron spectroscopy (HAXPES) measurements directly probe the density of states of energy levels around the valence band maximum of α-$SnWO_4$. By analyzing the impact of depositing NiO_x and SnO_2 on the surface of our pulsed laser deposited α-$SnWO_4$ films on the SPV and HAXPES data, we will show evidence that the previously proposed intraband states at the interface are indeed present and likely causing the photovoltage limitation.

2. Results and Discussion

First, SPV measurements (modulated illumination at 8 Hz) were performed on a pristine α-$SnWO_4$ film and on a film coated with a 20 nm-thick NiO_x layer. The structural, optoelectronic, and photoelectrochemical characterization of these films has been discussed in our previous reports.[10–13] **Figure 1**a shows the overall photovoltage amplitude R as a function of the photon energy for both films. Three qualitatively different ranges can be distinguished in the SPV spectra. At higher photon energies, i.e., above the bandgap of α-$SnWO_4$ (E_g, 1.9 eV[11]), the SPV signals are related to fundamental absorption, i.e., band-to-band excitation. In the range between about 1.6 and 1.85 eV, the SPV amplitude increases exponentially due to local potential fluctuations, which can be caused by disorders or local variations of the bandgap. The corresponding energies of the exponential tails (E_t) are about 65 and 70 meV for pristine and α-$SnWO_4$ films coated with 20 nm NiO_x, respectively. This means that local potential fluctuations increase near the surface of α-$SnWO_4$ after the deposition of NiO_x. At photon energies below ≈1.45 eV, the SPV amplitude increases to a maximum at about 0.85 eV and decreases to a minimum at about 1.45 eV. This means that photogeneration from deep defect states in the bandgap of α-$SnWO_4$ could lead, depending on the process of charge separation, to an increase or decrease of modulated charge separation.

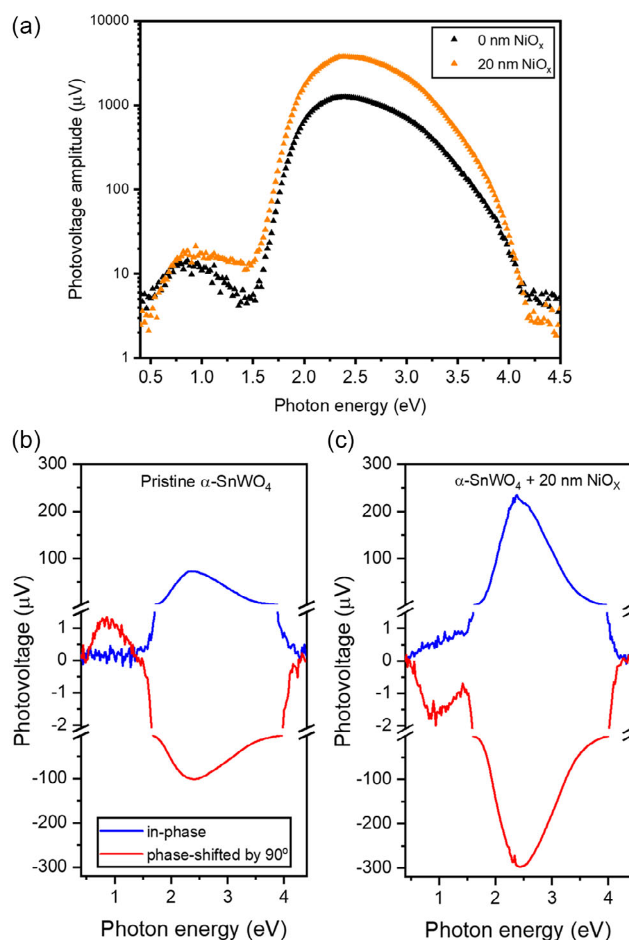

Figure 1. Surface photovoltage measurements (SPV) of pristine and α-$SnWO_4$ films coated with 20 nm NiO_x. a) Photovoltage amplitude of both films as a function of the excitation photon energy. In the low photon energy regime (below the bandgap of α-$SnWO_4$), the nonzero signal indicates the presence of surface or bulk defect states. In the high photon energy regime (above the bandgap), the amplitude increases after NiO_x deposition. Representation of the in-phase (blue) and phase-shifted by 90° (red) signals for b) the pristine α-$SnWO_4$ sample and c) the sample coated with 20 nm NiO_x. The deposition of 20 nm NiO_x clearly modifies the in-phase and phase shifted by 90° signals at sub-bandgap energies.

After the deposition of NiO_x, the SPV amplitude increases at photon energies above ≈0.75 eV but tends to decrease at lower photon energies. This suggests that modulated charge separation increases for photogeneration from deep defect states above about 0.75 eV as well as for excitation from tail states and for fundamental absorption. In contrast, the role of transitions leading to a decrease of modulated charge separation decreases after the deposition of NiO_x. The reduction of the SPV amplitude in a certain range below the bandgap has to be related to the reduction of the role of a certain kind of trap states at/near the surface. The separate analysis of the in-phase (X) and phase-shifted by 90° (Y) signals, from which the SPV amplitudes (R) are obtained (Equation (1)), allows us to distinguish more clearly the role of deep defect states for modulated charge separation

© 2023 The Authors. Solar RRL published by Wiley-VCH GmbH

2367198x, 0, Downloaded from https://onlinelibrary.wiley.com/doi/10.1002/solr.202201104 by Weizmann Institute Of Science, Wiley Online Library on [07/02/2023]. See the Terms and Conditions (https://onlinelibrary.wiley.com/terms-and-conditions) on Wiley Online Library for rules of use; OA articles are governed by the applicable Creative Commons License

2367198x, 0, Downloaded from https://onlinelibrary.wiley.com/doi/10.1002/solr.202201104 by Weizmann Institute Of Science, Wiley Online Library on [07/02/2023]. See the Terms and Conditions (https://onlinelibrary.wiley.com/terms-and-conditions) on Wiley Online Library for rules of use; OA articles are governed by the applicable Creative Commons License

$$R = \sqrt{X^2 + Y^2} \tag{1}$$

Here, it is important to mention that the *X*- and *Y*-signals are related to the fast and slow response with respect to the modulation period and that the relation between the signs of both gives information about the preferential direction of charge separation with regard to trapping.[26]

Figure 1b,c depicts the spectra of the *X*- and *Y*-signals of α-$SnWO_4$ before and after deposition of NiO_x, respectively. In the two regions above about 1.5 eV, all in-phase signals are positive and all phase shifted by 90° signals are negative. This is typical for charge separation of holes toward the surface and of electrons toward the bulk.[26] In the region below about 1.5 eV, the *X*-signals for the pristine film (i.e., before deposition of NiO_x) are practically zero whereas the *Y*-signals are positive. This means that electrons are partially trapped at surface states and that the relaxation time of detrapping is long in relation to the modulation period. In addition, above about 0.8 eV, the *Y*-signals decrease and change toward negative signals (change of sign at about 1.4 eV). This behavior can be interpreted as a reduction of electrons trapped at surface states due to photogeneration from defect states leading to the separation of holes toward the surface where they can recombine with electrons.

After the deposition of NiO_x, the behavior of the *X*- and *Y*- signals changes completely at photon energies below about 1.5 eV. First, positive *X*-signals appear and, second, the sign of the *Y*-signals changes to negative. This means that photogeneration from defect states leading to the separation of holes towards the surface dominates over photogeneration from defect states leading to the trapping of electrons at surface states and that the relaxation time of separated charge carriers decreased. Therefore, the deposition of NiO_x leads to a reduction of electron trapping at surface states and therefore to an increase of the overall SPV signal. This is attributed to increased band bending and enhanced charge separation, which agrees with our previous HAXPES measurements that demonstrated additional ≈0.4 eV band bending upon the deposition of NiO_x on α-$SnWO_4$.[12] Incidentally, photogeneration from defect states leading to preferential modulated separation of holes toward the surface may be attributed to sub-bandgap absorption via surface or bulk defect states.[27]

Overall, the SPV analyses suggest that a substantial modification of the charge generation, spatial redistribution, and relaxation in α-$SnWO_4$ films is introduced upon the deposition of the NiO_x layer. This is indicative of the creation and/or modification of defect states caused by the NiO_x deposition. In our previous studies, we showed that the deposition of NiO_x introduces the formation of Sn^{4+} species, most likely in the form of an SnO_2 layer, at the interface of α-$SnWO_4$ and NiO_x.[12] We therefore hypothesize that the origin of the sub-bandgap defect states or their modification observed in the SPV data is caused by the presence of this interfacial SnO_2 layer.

To test the earlier hypothesis, we performed another HAXPES investigation on two different samples: pristine α-$SnWO_4$ and SnO_2-coated α-$SnWO_4$. The SnO_2 layer was intentionally grown by photoelectrochemical oxidation of α-$SnWO_4$ at an applied potential of 1.23 V versus RHE in a 0.5 M KP_i buffer electrolyte (pH 7) with added 0.5 M Na_2SO_3. We have previously established that the integrated charge transfer from the initial current spike during this process can be assumed to fully contribute to the oxidation of $SnWO_4$.[11,12] Based on this, an SnO_2 layer thickness of ≈1 nm was estimated. By comparing the core level and valence band spectra of the two samples measured using hard X-rays, the chemical nature of the α-$SnWO_4$/SnO_2 interface could be studied.

Figure 2 shows the W 4*f* and Sn 3*d* core-level spectra of the pristine α-$SnWO_4$ sample (black) and the SnO_2-coated α-$SnWO_4$ sample (blue). Different photon energies (2210, 3880, and 6009 eV) were used, as indicated in the figure, to obtain depth-dependent information. The peak position of the nominal

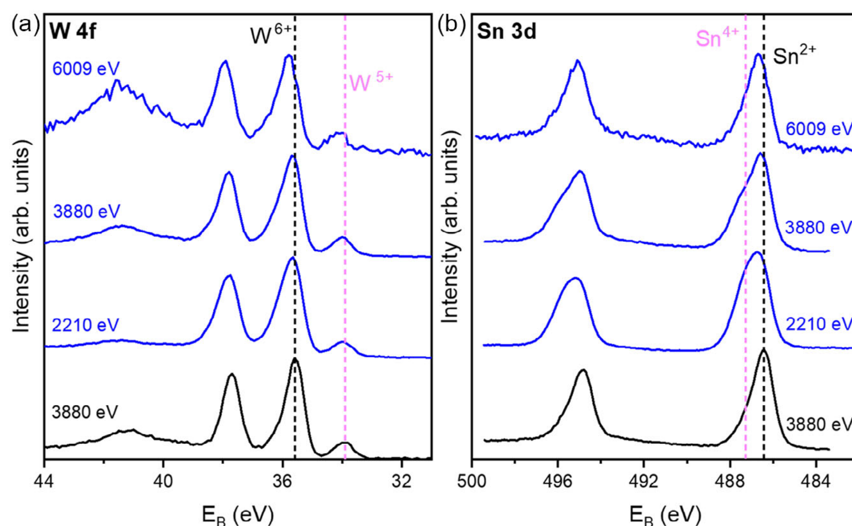

Figure 2. a) W 4*f* spectra of pristine α-$SnWO_4$ (black) and α-$SnWO_4$/SnO_2 (blue) samples measured by HAXPES. The varying excitation energies are indicated. The SnO_2 layer was formed by photoelectrochemical oxidation in 0.5 M KP_i + 0.5 M Na_2SO_3 (pH 7) using an applied potential of 1.23 V versus RHE, and the thickness is ≈1 nm. b) Sn 3*d* core level spectra measured by HAXPES. The oxidation of Sn^{2+} to Sn^{4+} can be observed by the peak asymmetry toward higher binding energy. Dashed vertical lines in (a) and (b) indicate the peak positions of W^{5+}, W^{6+}, Sn^{2+}, and Sn^{4+}.

© 2023 The Authors. Solar RRL published by Wiley-VCH GmbH

oxidation state of W in α-$SnWO_4$ (W^{6+}) is indicated in Figure 2a by the dashed vertical black line. In addition, a small W^{5+} contribution is observed and indicated by the dashed vertical magenta line. This observation of W^{5+} agrees with our earlier work where it was discussed in more detail.[12] A comparison of the W 4*f* spectrum of the pristine sample and the SnO_2-coated samples reveals a spectral broadening (see Figure S1, Supporting Information for the quantitative full-width at half-maximum, FWHM, of the W $4f_{5/2}$ peak). This increase in FWHM can be attributed to an additional W^{6+} contribution not related to the α-$SnWO_4$ phase. For example, the formation of WO_3, which was suggested earlier as a possible degradation product,[11] may be the origin of this additional W^{6+} species. It should be noted, however, that changes in band bending can also contribute to the broadening of the peak. Note that the earlier FWHM analysis was done for W $4f_{5/2}$ peak, since the contribution from W^{5+} overlaps with the lower binding energy peak of W $4f_{7/2}$, but not the W $4f_{5/2}$ peak.

The Sn 3*d* core-level spectra shown in Figure 2b show a clear peak asymmetry toward higher binding energies after the introduction of SnO_2, due to spectral contribution from Sn^{4+}. When varying the probing depth, we also observe a variation in the Sn^{4+} contribution. For larger probing depths (i.e., higher photon energy), the Sn^{4+} contribution is lower, which indicates that Sn remains in the 2+ oxidation state in the underlying α-$SnWO_4$ film. HAXPES measurements were also performed on an α-$SnWO_4$ sample coated with a thicker layer of SnO_2 (≈12.5 nm), and the same trends are revealed (see Figure S1 and S2, Supporting Information).

A quantitative analysis of the relative contributions of the different species and their binding energies is reported in **Figure 3**. As described in the Experimental Section, the analysis was performed by a peak-fitting procedure, and an example of the fitted spectra for the pristine α-$SnWO_4$ film can be found in Figure S3, Supporting Information. The relative W^{5+} contribution is shown in Figure 3a as a function of the photon energy for α-$SnWO_4$ films coated with SnO_2 layers of two different thicknesses: ≈1 and ≈12.5 nm. The contribution of W^{5+} in both samples increases with increasing photon energy, and the overall W^{5+} contribution is higher for the sample with the 1 nm SnO_2 layer. These observations suggest that the W^{5+} contribution originates from the bulk of the α-$SnWO_4$ film, which agrees with our earlier discussion.[12] In contrast, a decrease of the Sn^{4+} contribution with increasing photon energies can be seen in Figure 3b. This is expected since the intentionally grown SnO_2 layer, which contains the Sn^{4+} species, is present on the surface. The overall higher contribution of Sn^{4+} and the steeper decrease with increasing photon energy observed for the sample with a 12.5 nm-thick SnO_2 layer are also consistent with the explanation above. For comparison, the W^{5+} and Sn^{4+} contributions in the

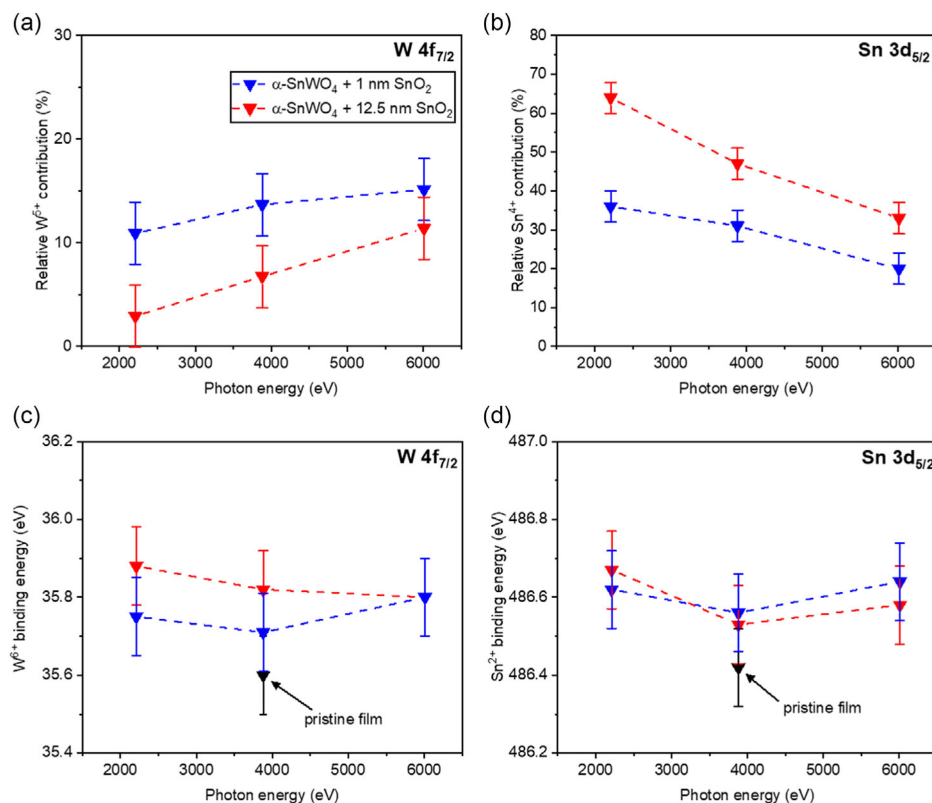

Figure 3. Analysis of the core-level spectra for the α-$SnWO_4$ + 1 nm SnO_2 (blue data points) and α-$SnWO_4$ + 12.5 nm SnO_2 (red data points) samples (the spectra are shown in Figure 2 and Figure S2, Supporting Information, respectively). a) Relative W^{5+} contribution extracted from the W $4f_{7/2}$ peak. b) Relative Sn^{4+} contribution extracted from the Sn $3d_{5/2}$ peak. c) Binding energies of the W^{6+} species (W $4f_{7/2}$ peak). d) Binding energies of the Sn^{2+} species (Sn $3d_{5/2}$ peak). The respective binding energies of the pristine sample are also indicated in (c) and (d) by the black data point.

© 2023 The Authors. Solar RRL published by Wiley-VCH GmbH

2367198x, 0, Downloaded from https://onlinelibrary.wiley.com/doi/10.1002/solr.202201104 by Weizmann Institute Of Science, Wiley Online Library on [07/02/2023]. See the Terms and Conditions (https://onlinelibrary.wiley.com/terms-and-conditions) on Wiley Online Library for rules of use; OA articles are governed by the applicable Creative Commons License

2367198x, 0, Downloaded from https://onlinelibrary.wiley.com/doi/10.1002/solr.202201104 by Weizmann Institute Of Science, Wiley Online Library on [07/02/2023]. See the Terms and Conditions (https://onlinelibrary.wiley.com/terms-and-conditions) on Wiley Online Library for rules of use; OA articles are governed by the applicable Creative Commons License

pristine α-$SnWO_4$ sample are estimated to be $10 \pm 3\%$ and $19 \pm 4\%$, respectively, from the spectra at the photon energy of 3880 eV.

Figure 3c,d plots the binding energies of W^{6+} and Sn^{2+} (nominal oxidation states of W and Sn in α-$SnWO_4$) as a function of the photon energy. The binding energies remain rather constant with increasing photon energy, and a small increase of the binding energies can be observed for the SnO_2-coated samples in comparison to the pristine film. While this may be attributed to changes in band bending related to the presence of the SnO_2 layer, the distribution of values falls within the experimental error range of $\pm$0.1 eV. Thus, we conclude that no major changes are observed for the W^{6+} and Sn^{2+} binding energies upon the formation of SnO_2.

Valence band measurements were then performed on the pristine α-$SnWO_4$ and α-$SnWO_4/SnO_2$ samples. The valence band spectra recorded with a photon energy of 3933 eV are shown in **Figure** 4a. Note that the spectra are reported with the intensity axis on a logarithmic scale and are normalized to the peak maximum centered at $\approx$2.8 eV. Evaluation of the valence band maximum (VBM) shows that the VBM of α-$SnWO_4$ appears as expected at 1.5 ± 0.1 eV (see Figure S4, Supporting Information). This value agrees well with the earlier report of 1.6 ± 0.1 eV determined by ultraviolet photoelectron spectroscopy (UPS).[11] When comparing the pristine sample with the α-$SnWO_4/SnO_2$ samples, two differences are noted. First, an increase in the intensity at higher binding energies (>4 eV) is observed for the α-$SnWO_4/SnO_2$ samples. The intensity increases with the thickness of SnO_2, which suggests that this change may originate from the valence band spectra of the SnO_2 layer. Indeed, SnO_2 is a large bandgap semiconductor with a reported VBM at >3 eV binding energy.[28–30] Second, an additional feature emerges at the binding energy of $\approx$0.5–1.5 eV (peak at $\approx$0.7 eV) for the α-$SnWO_4/SnO_2$ samples. This energy range is within the bandgap of α-$SnWO_4$ and is therefore assigned to an intraband defect state. The intensity of this feature remains the same for the samples with 1 and 12.5 nm-thick layers of SnO_2, thereby suggesting that its origin is not related to the SnO_2 layer itself, but it most likely arises from the α-$SnWO_4/SnO_2$ interface. Based on the valence band spectra, a schematic band diagram of the α-$SnWO_4/SnO_2$ interface region is constructed and shown in Figure 4b. The approximate locations of the energy levels and the defect state in the bandgap of α-$SnWO_4$ are indicated.

We can now combine the findings from the HAXPES investigation with the SPV data. The binding energy range of the intraband defect state observed in the HAXPES VB measurements agrees very well with the sub-bandgap signals observed in the SPV data. In addition, the relatively low intensity of the sub-bandgap signals in the SPV data is also consistent with the hypothesis that they originate from an intraband defect state at the interface. We note that a direct correlation cannot be made, since the SPV measurements were performed using α-$SnWO_4/NiO_x$ samples, while α-$SnWO_4/SnO_2$ samples were used for the HAXPES measurements. Unfortunately, HAXPES valence band measurements directly on the α-$SnWO_4/NiO_x$ samples are unable to reveal the intraband defect state since its energy overlaps directly with the VBM of NiO_x (see Figure S5, Supporting Information). Note that the density of states in the VBM of NiO_x

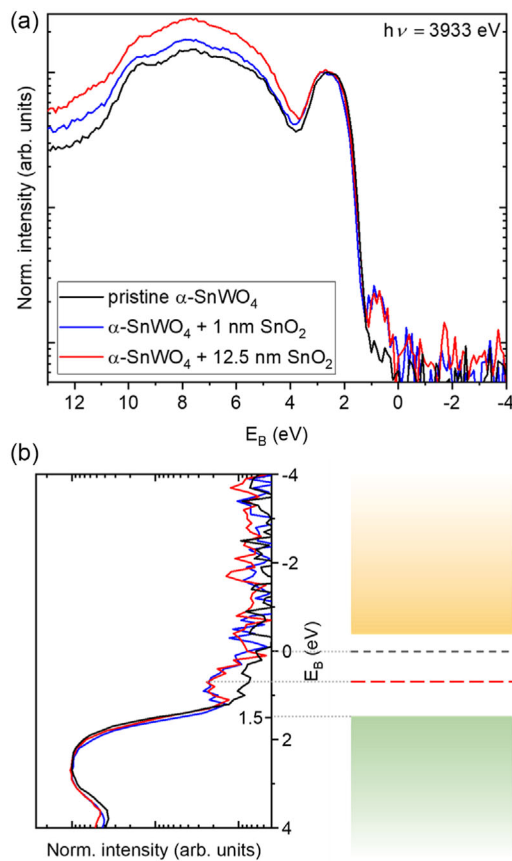

Figure 4. a) HAXPES valence band spectra of the pristine α-$SnWO_4$, α-$SnWO_4$ + 1 nm SnO_2, and α-$SnWO_4$ + 12.5 nm SnO_2 samples. The spectra were normalized to the peak maximum at $\approx$2.8 eV. After formation of SnO_2, an indication for an additional state above the valence band maximum (VBM) can be observed. b) A schematic band diagram is depicted based on the valence band spectra in (a) (rotated here). The approximate location of the state E_D within the bandgap E_g of α-$SnWO_4$ is shown, along with other energy levels: E_F = Fermi level, E_C = conduction band minimum, and E_V = valence band maximum. The position of E_V was determined from the nonlogarithmic plot, as shown in Figure S4, Supporting Information.

is much higher, and therefore masks that of the intraband defect state. However, since it was already established that an interfacial layer (SnO_2) forms between α-$SnWO_4$ and NiO_x,[12] and SPV measurement on a α-$SnWO_4/SnO_2$ sample also shows sub-bandgap signals (Figure S6, Supporting Information), we postulate that the sub-bandgap signals observed in the SPV data of α-$SnWO_4/NiO_x$ originate from the same intraband defect state that we observed in the HAXPES measurements of α-$SnWO_4/SnO_2$. Indeed, the defect structures of SnO_2 and SnO_x have been investigated in several studies,[31–36] and the origin of the observed intraband states has been correlated with the presence of oxygen vacancies. Thus, oxygen vacancies in the SnO_2 layer are likely to be responsible for the intraband defect states observed in our study. Thus, we attribute the reduction in photovoltage observed in earlier studies,[11,12] which manifests itself in the form of Fermi-level pinning (see Figure S7, Supporting Information for band diagram illustration), to the defective

© 2023 The Authors. Solar RRL published by Wiley-VCH GmbH

nature of the oxidized (SnO_2) layer at the interface of α-$SnWO_4$ and NiO_x.

3. Conclusion

In summary, we have successfully detected the presence of an intraband state in α-$SnWO_4$ films covered with oxide overlayers. SPV spectroscopy measurements on NiO_x-coated α-$SnWO_4$ show higher photovoltage amplitudes compared with the pristine film at photon energies above and below the bandgap of α-$SnWO_4$. The former is attributed to increased band bending, while the sub-bandgap signals can be explained by the presence of an intraband defect state as a result of NiO_x deposition. To confirm whether the intraband defect state is truly present at the interface, valence band measurements using HAXPES were performed. Since our earlier investigation has shown that the deposition of NiO_x on α-$SnWO_4$ introduces an interfacial oxide layer likely to be SnO_2,[12] and detecting the intraband state on NiO_x-coated samples is hindered by the overlapping signals from the NiO_x overlayer, we have intentionally grown a thin SnO_2 layer on the surface of our α-$SnWO_4$ films by performing a photoelectrochemical oxidation treatment. HAXPES analyses were then performed to further examine the interface between α-$SnWO_4$ and SnO_2. The formation of the SnO_2 layer is confirmed by the increase of the Sn^{4+} contribution in the Sn 3d core-level spectra. More importantly, valence band measurements of the SnO_2-coated α-$SnWO_4$ films reveal the presence of an intraband state ≈0.7 eV above the VBM; this state is not detected in the pristine film. The signal intensity corresponding to this state does not change with increasing SnO_2 thickness, indicating that it originates from the interface between α-$SnWO_4$ and SnO_2. Interestingly, the energetic position of the intraband state detected by HAXPES agrees very well with the sub-bandgap signals observed in the SPV analysis of NiO_x-coated α-$SnWO_4$, consistent with the presence of an SnO_2 layer at the α-$SnWO_4$/NiO_x interface. Consequently, the origin of Fermi-level pinning, which was previously shown to limit the photovoltage that can be extracted from NiO_x-coated α-$SnWO_4$ photoanodes,[11,12] can be explained by the presence of an intraband state at the α-$SnWO_4$/oxide interface.

4. Experimental Section

Thin-Film Preparation: The α-$SnWO_4$ films were prepared by pulsed laser deposition (PLD) as reported previously.[10–13] As the substrate material, a fluorine-doped tin oxide-coated glass (FTO TEC 7, Pilkington) was used, which was cut into pieces of approximately 24 × 24 mm^2. Before film deposition, the substrates were cleaned in five successive 15 min ultrasonic bath treatments using different solutions, starting with 1 vol% Triton solution (Triton X-100, laboratory grade, Sigma-Aldrich), followed by acetone, propanol, ethanol, and deionized water (Milli-Q, 18.2 MΩ cm). Subsequently, the substrates were dried under an N_2 gas stream. A custom-made α-$SnWO_4$ target was ablated in a custom-built PLD system (PREVAC, Poland). The preparation procedure of the α-$SnWO_4$ target has been reported previously.[11] A KrF-excimer pulsed laser (wavelength $\lambda = 248$ nm, LPXpro 210, Coherent) was focused on the target located in the preparation chamber. The base pressure in the chamber was 10^{-7} mbar. During deposition, O_2 gas was used as the process gas such that the pressure in the chamber was increased to $\approx 10^{-4}$ mbar. Target ablation was performed with a laser repetition rate of 10 Hz and a fluence of 2 J cm^{-2}. The laser beam spot size was 1.3 × 2 mm^2. Between the target and the substrate, a distance of 60 mm was set. In order to achieve a homogeneous film thickness, the substrate was rotated at 12° s^{-1} (2 rpm). After the films were deposited at room temperature, the samples were annealed at 520 °C for 2 h in a tube furnace under argon flow to obtain the crystalline α-$SnWO_4$ phase.

The NiO_x layers were deposited on the α-$SnWO_4$ films using the same PLD setup. A metallic Ni target (99.99%, Alfa Aesar) was used for film deposition at room temperature. An O_2 process gas (0.05 mbar chamber pressure) was used to deposit the NiO_x layer in a reactive deposition process. The laser fluence was 2 J cm^{-2}, and the laser repetition rate was 10 Hz. The target rotation was set to 12° s^{-1} (2 rpm), and the target-to-substrate distance was 60 mm.

The SnO_2 layers were formed by photoelectrochemical oxidation of the α-$SnWO_4$ samples. For that purpose, the samples were mounted in a custom-made Teflon cell and a potential of 1.23 V versus RHE was applied with an EG&G Princeton Applied Research (Model 273A) potentiostat. A three-electrode configuration was used with an Ag/AgCl reference electrode (XR300, KCl saturated, Radiometer Analytics) and a coiled Pt wire acting as the counter electrode. Sunlight was simulated with a WACOM super solar simulator (Model WXS-505-5 h, AM 1.5, Class AAA). The film oxidation was performed in a 0.5 M KP_i buffer (pH 7) electrolyte, containing 0.5 M Na_2SO_3 as hole scavenger.

Surface Photovoltage Measurements: Modulated SPV spectra were measured in a parallel plate capacitor configuration, composed of a quartz cylinder partially coated with the SnO_2:F electrode, and a mica sheet as an insulator.[37] The measurements were performed at ambient conditions. The SPV signal is recorded as a change in the surface potential as a result of the illumination. Illumination from the front (i.e., light impinging the surface of the sample) was provided by a halogen lamp, coupled to a quartz prism monochromator (SPM2) and modulated at a frequency of 8 Hz using an optical chopper. The in-phase and phase-shifted by 90° SPV signals were detected with a high-impedance buffer and a dual phase lock-in amplifier (EG&G 5210). The photovoltage amplitude is defined as the square root of the sum of the squared in-phase and 90° phase-shifted SPV signals,[38] as defined in Equation (1). A more detailed description of the SPV setup, including the schematic and the specific roles of each components, has been reported in the literature.[26,37,38] Finally, additional discussion on the role of straylight and how it affects the sub-bandgap signals, as well as the consideration for choosing the modulation frequency, can be found in Supporting Information Note S1.

Hard X-ray Photoelectron Spectroscopy: The surface analysis of the α-$SnWO_4$ and α-$SnWO_4$/SnO_2 samples was performed at the BESSY II synchrotron at Helmholtz-Zentrum Berlin, Germany. The measurements were performed at the KMC-1 beamline with the HIKE (high kinetic energy photoemission) end-station.[39,40] Photon energies of 2210, 3880, 3933, and 6009 eV were used for the measurements and adjusted with Si (111) and Si (311) double crystal monochromator planes. The photoelectrons emitted from the samples were detected with a Scienta R4000 electron spectrometer. Core level and valence band spectra were recorded with a step size of 0.1 eV and the pass energy was set to 200 eV. The base pressure of the analysis chamber was $\approx 10^{-8}$ mbar. The calibration of the binding energy scale was done by acquiring the Au 4$f_{7/2}$ core level from a gold foil attached on the sample holder and in electrical contact with the sample. The Au 4$f_{7/2}$ core-level binding energy was set to 84.00 eV. During the measurements, a common ground was established between the sample and the electron spectrometer. Quantitative analysis of the peaks was performed with a peak fitting procedure. Prior to that, a Shirley baseline correction was performed. Pseudo-Voigt functions (e.g., linear combination of Gaussian and Lorentzian functions) were used for the procedure. Finally, chi-square minimization was performed to obtain the fitted spectra.

Supporting Information

Supporting Information is available from the Wiley Online Library or from the author.

© 2023 The Authors. Solar RRL published by Wiley-VCH GmbH

2367198x, 0, Downloaded from https://onlinelibrary.wiley.com/doi/10.1002/solr.202201104 by Weizmann Institute Of Science, Wiley Online Library on [07/02/2023]. See the Terms and Conditions (https://onlinelibrary.wiley.com/terms-and-conditions) on Wiley Online Library for rules of use; OA articles are governed by the applicable Creative Commons License

2367198x, 0, Downloaded from https://onlinelibrary.wiley.com/doi/10.1002/solr.202201104 by Weizmann Institute Of Science, Wiley Online Library on [07/02/2023]. See the Terms and Conditions (https://onlinelibrary.wiley.com/terms-and-conditions) on Wiley Online Library for rules of use; OA articles are governed by the applicable Creative Commons License

Acknowledgements

The authors acknowledge financial support for this work from the Helmholtz International Research School "Hybrid Integrated Systems for Conversion of Solar Energy" (HI-SCORE), an initiative co-funded by the Initiative and Networking Fund of the Helmholtz Association. They would also like to thank Roberto Felix Duarte for the access and technical assistance to the HiKE end-station, KMC-1 beamline at the BESSY-II synchrotron facility.

Open Access funding enabled and organized by Projekt DEAL.

Conflict of Interest

The authors declare no conflict of interest.

Author Contributions

P.S. prepared the α-$SnWO_4$, α-$SnWO_4$/NiO_x, and α-$SnWO_4$/SnO_2 samples. P.S. and F.F.A. wrote the initial version of the manuscript, which was revised with the help of contributions by all authors. T.D. performed the SPV measurements and supported with the data analysis and interpretation. P.S., E.F, K.O., J.V.R., and F.F.A. performed the HAXPES measurements at BESSY II at Helmholtz-Zentrum Berlin, Germany. P.S., M.F., R.v.d.K., and F.F.A. planned the study and contributed to the data interpretation.

Data Availability Statement

The data that support the findings of this study are available from the corresponding author upon reasonable request.

Keywords

complex metal oxides, photoanodes, photoemission spectroscopy, $SnWO_4$, surface photovoltage spectroscopy

Received: December 14, 2022
Revised: January 11, 2023
Published online:

[1] R. van de Krol, M. Grätzel, *Photoelectrochemical Hydrogen Production*, Springer, New York, NY **2012**.
[2] L. M. Peter, K. G. Upul Wijayantha, *ChemPhysChem* **2014**, *15*, 1983.
[3] M. G. Walter, E. L. Warren, J. R. McKone, S. W. Boettcher, Q. Mi, E. A. Santori, N. S. Lewis, *Chem. Rev.* **2010**, *110*, 6446.
[4] J. H. Kim, D. Hansora, P. Sharma, J.-W. Jang, J. S. Lee, *Chem. Soc. Rev.* **2019**, *48*, 1908.
[5] M. J. Kenney, M. Gong, Y. Li, J. Z. Wu, J. Feng, M. Lanza, H. Dai, *Science* **2013**, *342*, 836.
[6] O. Khaselev, J. A. Turner, *Science* **1998**, *280*, 425.
[7] F. F. Abdi, S. P. Berglund, *J. Phys. D: Appl. Phys.* **2017**, *50*, 193002.
[8] K. Sivula, R. van de Krol, *Nat. Rev. Mater.* **2016**, *1*, 15010.
[9] D. K. Lee, D. Lee, M. A. Lumley, K.-S. Choi, *Chem. Soc. Rev.* **2019**, *48*, 2126.
[10] M. Kölbach, H. Hempel, K. Harbauer, M. Schleuning, A. Petsiuk, K. Höflich, V. Deinhart, D. Friedrich, R. Eichberger, F. F. Abdi, R. van de Krol, *ACS Appl. Energy Mater.* **2020**, *3*, 4320.
[11] M. Kölbach, I. J. Pereira, K. Harbauer, P. Plate, K. Höflich, S. P. Berglund, D. Friedrich, R. van de Krol, F. F. Abdi, *Chem. Mater.* **2018**, *30*, 8322.
[12] P. Schnell, M. Kölbach, M. Schleuning, K. Obata, R. Irani, I. Y. Ahmet, M. Harb, D. E. Starr, R. van de Krol, F. F. Abdi, *Adv. Energy. Mater.* **2021**, *11*, 2003183.
[13] P. Schnell, J. M. C. M. Dela Cruz, M. Kölbach, R. van de Krol, F. F. Abdi, *Chem. Mater.* **2022**, *34*, 1590.
[14] Z. Zhu, P. Sarker, C. Zhao, L. Zhou, R. L. Grimm, M. N. Huda, P. M. Rao, *ACS Appl. Mater. Interf.* **2017**, *9*, 1459.
[15] F. Bozheyev, E. M. Akinoglu, L. Wu, H. Lu, R. Nemkayeva, Y. Xue, M. Jin, M. Giersig, *Int. J. Hydrog. Energy* **2020**, *45*, 8676.
[16] A. Ziani, M. Harb, D. Noureldine, K. Takanabe, *APL Mater.* **2015**, *3*, 096101.
[17] M. Harb, A. Ziani, K. Takanabe, *Phys. Status Solidi B* **2016**, *253*, 1115.
[18] Y. Liu, W. Qiu, G. He, K. Wang, Y. Wang, L. Chen, Q. Wu, W. Li, J. Li, *J. Phys. Chem. C* **2022**, *126*, 15596.
[19] G. He, W. Li, W. Qiu, C. Xu, K. Wang, L. Chen, Y. Wang, Y. Liu, J. Li, *ACS Appl. Energy Mater.* **2022**, *5*, 11883.
[20] W. Qiu, Y. Zhang, G. He, L. Chen, K. Wang, Q. Wang, W. Li, Y. Liu, J. Li, *ACS Appl. Energy Mater.* **2022**, *5*, 11732.
[21] S. Zhu, D. Liu, J. Li, Y. Kuang, *ACS Appl. Energy Mater.* **2022**, *5*, 14372.
[22] D. Liu, X. Chen, Y. Qiao, Y. Zhou, Y. Kuang, *Adv. Energy Sustainability Res.* **2022**, *3*, 2100146.
[23] I.-S. Cho, C. H. Kwak, D. W. Kim, S. Lee, K. S. Hong, *J. Phys. Chem. C* **2009**, *113*, 10647.
[24] R. Gottesman, I. Peracchi, J. L. Gerke, R. Irani, F. F. Abdi, R. van de Krol, *ACS Energy Lett.* **2022**, *7*, 514.
[25] B. Huang, J. N. Hart, *Phys. Chem. Chem. Phys.* **2020**, *22*, 1727.
[26] T. A. Dittrich, S. Fengler, *Surface Photovoltage Analysis of Photoactive Materials*, World Scientific, London, UK **2019**.
[27] L. Kronik, Y. Shapira, *Surf. Sci. Rep.* **1999**, *37*, 1.
[28] M. A. Stranick, A. Moskwa, *Surf. Sci. Spectra* **1993**, *2*, 50.
[29] C. Ke, W. Zhu, Z. Zhang, E. Soon Tok, B. Ling, J. Pan, *Sci. Rep.* **2015**, *5*, 17424.
[30] L. Lin, T. W. Jones, J. T.-W. Wang, A. Cook, N. D. Pham, N. W. Duffy, B. Mihaylov, M. Grigore, K. F. Anderson, B. C. Duck, H. Wang, J. Pu, J. Li, B. Chi, G. J. Wilson, *Small* **2020**, *16*, 1901466.
[31] L. Grządziel, M. Krzywiecki, A. Szwajca, A. Sarfraz, G. Genchev, A. Erbe, *J. Phys. D Appl. Phys.* **2018**, *51*, 315301.
[32] D. F. Cox, T. B. Fryberger, S. Semancik, *Phys. Rev. B* **1988**, *38*, 2072.
[33] J. Haeberle, S. Machulik, C. Janowitz, R. Manzke, D. Gaspar, P. Barquinha, D. Schmeißer, *J. Appl. Phys.* **2016**, *120*, 105101.
[34] J. M. Themlin, R. Sporken, J. Darville, R. Caudano, J. M. Gilles, R. L. Johnson, *Phys. Rev. B* **1990**, *42* 11914.
[35] F. Trani, M. Causà, D. Ninno, G. Cantele, V. Barone, *Phys. Rev. B* **2008**, *77*, 245410.
[36] Ç. Kılıç, A. Zunger, *Phys. Rev. Lett.* **2002**, *88*, 095501.
[37] T. Dittrich, A. Gonzáles, T. Rada, T. Rissom, E. Zillner, S. Sadewasser, M. Lux-Steiner, *Thin Solid Films* **2013**, *535*, 357.
[38] V. Duzhko, V. Y. Timoshenko, F. Koch, T. Dittrich, *Phys. Rev. B* **2001**, *64*, 075204.
[39] M. Gorgoi, S. Svensson, F. Schäfers, G. Öhrwall, M. Mertin, P. Bressler, O. Karis, H. Siegbahn, A. Sandell, H. Rensmo, W. Doherty, C. Jung, W. Braun, W. Eberhardt, *Nucl. Instrum. Methods Phys. Res. Sect. A* **2009**, *601* 48.
[40] F. Schaefers, M. Mertin, M. Gorgoi, *Rev. Sci. Instrum.* **2007**, *78* 123102.

© 2023 The Authors. Solar RRL published by Wiley-VCH GmbH